

METAL-POOR STARS OBSERVED WITH THE MAGELLAN TELESCOPE. III.¹ NEW EXTREMELY AND ULTRA METAL-POOR STARS FROM SDSS/SEGUE AND INSIGHTS ON THE FORMATION OF ULTRA METAL-POOR STARS

VINICIUS M. PLACCO², ANNA FREBEL³, YOUNG SUN LEE⁴, HEATHER R. JACOBSON³,
 TIMOTHY C. BEERS², JOSE M. PEN³, CONRAD CHAN⁵, ALEXANDER HEGER^{5,6,7}

Draft version July 15, 2015

ABSTRACT

We report the discovery of one extremely metal-poor (EMP; $[\text{Fe}/\text{H}] < -3$) and one ultra metal-poor (UMP; $[\text{Fe}/\text{H}] < -4$) star selected from the SDSS/SEGUE survey. These stars were identified as EMP candidates based on their medium-resolution ($R \sim 2,000$) spectra, and were followed-up with high-resolution ($R \sim 35,000$) spectroscopy with the Magellan-Clay Telescope. Their derived chemical abundances exhibit good agreement with those of stars with similar metallicities. We also provide new insights on the formation of the UMP stars, based on comparison with a new set of theoretical models of supernovae nucleosynthesis. The models were matched with 20 UMP stars found in the literature, together with one of the program stars (SDSS J1204+1201), with $[\text{Fe}/\text{H}] = -4.34$. From fitting their abundances, we find that the supernovae progenitors, for stars where carbon and nitrogen are measured, had masses ranging from $20.5 M_{\odot}$ to $28 M_{\odot}$, and explosion energies from 0.3 to 0.9×10^{51} erg. These results are highly sensitive to the carbon and nitrogen abundance determinations, which is one of the main drivers for future high-resolution follow-up of UMP candidates. In addition, we are able to reproduce the different CNO abundance patterns found in UMP stars with a single progenitor type, by varying its mass and explosion energy.

Keywords: Galaxy: halo—techniques: spectroscopy—stars: abundances—stars: atmospheres—stars: Population II—stars: individual (SDSS J1204+1201)—stars: individual (SDSS J1322+0123)

1. INTRODUCTION

The most metal-poor stars in the Galactic halo carry important information about the formation and early evolution of the conditions in the early universe, as well as in the assembly of the Milky Way. In particular, ultra metal-poor (UMP; $[\text{Fe}/\text{H}]^8 < -4.0$, e.g., Beers & Christlieb 2005; Frebel & Norris 2013) stars are believed to be formed by gas clouds polluted by the chemical yields of the very first (Population III) stars formed in the universe (Iwamoto et al. 2005). Even though this scenario for the origin of UMP stars is qualitatively widely accepted, there are still many open questions, such as the range of masses and specific characteristics of the population of first stars, and how many progenitors each UMP star might have had (Tominaga et al. 2014).

There are different scenarios for the progenitor pop-

ulations that have been proposed to provide the necessary ingredients to trigger the formation of UMP stars: (i) pair-instability supernovae from very massive stars (e.g., Heger & Woosley 2002), however, the predicted abundance pattern from such supernova has not been uniquely observed; (ii) relatively normal massive stars, however, with reduced mixing relative to their modern counterparts (e.g., Heger & Woosley 2010); (iii) Fast-rotating massive stars (Meynet et al. 2006, 2010) and; (iv) “Faint” supernovae (Nomoto et al. 2006, 2013; Keller et al. 2014). Analyses of the abundances of UMP stars, however, are required to ultimately establish the nature and shape of the initial mass function (IMF) of these Population III stars. The goal is to constraint the progenitor properties including their masses (see discussion in Placco et al. 2014a). Presently, however, there are about 20 UMP stars with high-resolution spectra available in the literature, and only five stars known to be hyper metal-poor (HMP; $[\text{Fe}/\text{H}] \leq -5.0$, Frebel et al. 2015; Bonifacio et al. 2015; Christlieb et al. 2002; Frebel et al. 2005; Keller et al. 2014).

Since the completion of the Sloan Extension for Galactic Understanding and Exploration (SEGUE-1; Yanny et al. 2009) and SEGUE-2 (Rockosi et al. 2015), the numbers of identified Very/Extremely metal-poor (VMP/EMP, with $[\text{Fe}/\text{H}] < -2.0$ and < -3.0 , respectively) stars have increased by over an order of magnitude, when compared to previous efforts, such as the HK (Beers et al. 1985, 1992) and Hamburg/ESO (Christlieb et al. 2008) surveys. The SEGUE-1 and SEGUE-2 campaigns, sub-surveys of the Sloan Digital Sky Survey (SDSS; York et al. 2000), accomplished this with

¹ Based on observations gathered with the 6.5 m Magellan Telescopes located at Las Campanas Observatory, Chile

² Department of Physics and JINA Center for the Evolution of the Elements, University of Notre Dame, Notre Dame, IN 46556, USA

³ Department of Physics and Kavli Institute for Astrophysics and Space Research, Massachusetts Institute of Technology, Cambridge, MA 02139, USA

⁴ Department of Astronomy and Space Science, Chungnam National University, Daejeon 305-764, Republic of Korea

⁵ Monash Centre for Astrophysics, School of Physics and Astronomy, 19 Rainforest Walk, Monash University, Vic 3800, Australia

⁶ Shanghai Jiao-Tong University, CNA, Department of Physics and Astronomy, Shanghai 200240, P. R. China

⁷ University of Minnesota, School of Physics and Astronomy, Minneapolis, MN 55455, USA

⁸ $[A/B] = \log(N_A/N_B)_* - \log(N_A/N_B)_{\odot}$, where N is the number density of atoms of a given element in the star ($*$) and the Sun (\odot), respectively.

medium-resolution ($R \sim 2,000$) spectroscopy. Currently, there are several tens of thousands of VMP (and on the order of 1000 EMP) candidates identified by these surveys, but just a small fraction have been studied with high-resolution spectroscopy. Recent efforts to increase these numbers using SDSS/SEGUE candidates include studies by Caffau et al. (2011b), Bonifacio et al. (2012, 2015), Frebel et al. (2015), and Aoki et al. (2013), and have already resulted in the discovery of SDSS J1029+1729, with $[\text{Fe}/\text{H}] = -4.99$ (Caffau et al. 2011a), SDSS J1742+2531, with $[\text{Fe}/\text{H}] = -4.80$ and SDSS J1035+0641, with $[\text{Fe}/\text{H}] < -5.07$ (Bonifacio et al. 2015), and SDSS J1313+0019, with $[\text{Fe}/\text{H}] = -5.00$ (Allende Prieto et al. 2015; Frebel et al. 2015).

In this paper, we present results from a new selection effort for EMP stars from the data base of medium-resolution SDSS/SEGUE spectra. We report the discovery of another UMP star, SDSS J120441.39+120111.5 (hereafter SDSS J1204+1201, $[\text{Fe}/\text{H}] = -4.34 \pm 0.05$) and also an EMP star, SDSS J132250.60+012343.0 (hereafter SDSS J1322+0123, $[\text{Fe}/\text{H}] = -3.64 \pm 0.05$), selected from medium-resolution SDSS/SEGUE spectra. We have carried out a detailed chemical-abundance analysis, as well as a comparison with data from the literature and theoretical models for Population III stars, in order to gain insights on the progenitor population(s) of UMP stars. This paper is outlined as follows: Section 2 describes the medium-resolution spectroscopy target selection and high-resolution follow-up observations, followed by the determinations of the stellar parameters and chemical abundances in Section 3. Section 4 shows a comparison between (i) the abundances of the program stars and other literature data, and (ii) the UMP stars in the literature and a new set of theoretical models for Pop III stars. Our conclusions are provided in Section 5.

2. TARGET SELECTION AND OBSERVATIONS

Our targets were selected from the SEGUE-2 database, to avoid possible overlap with other high-resolution surveys of metal-poor stars based on SDSS/SEGUE data. We applied restrictions to the magnitude ($g < 16.8$) and metallicity ($[\text{Fe}/\text{H}] < -3.0$). Estimates of the stellar atmospheric parameters from medium-resolution SDSS/SEGUE spectra were obtained using the SEGUE Stellar Parameter Pipeline (SSPP - see Lee et al. 2008a,b; Allende Prieto et al. 2008; Smolinski et al. 2011; Lee et al. 2011, 2013, for a detailed description). These restrictions cut down the entire SDSS/SEGUE sample to ten potential UMP stars. Although there are many more possible EMP star candidates selected from the SDSS/SEGUE-2, we imposed the magnitude constraint in order to obtain candidates which can be observed with high signal-to-noise, sufficient for detailed high-resolution spectral analysis, at reasonable exposure times. After visual inspection of the ten candidate spectra (and checking their atmospheric parameters from the SSPP), two objects were followed-up: SDSS J1204+1201 and SDSS J1322+0123, which were the lowest metallicity candidates. Table 1 lists basic information on the program stars. Table 2 lists the SSPP-derived T_{eff} , $\log g$, and $[\text{Fe}/\text{H}]$, used as first-pass estimates when determining the parameters for the high-resolution analysis, presented in Section 3.

Figure 1 shows the SDSS/SEGUE-2 spectra for the observed stars, in comparison with the star

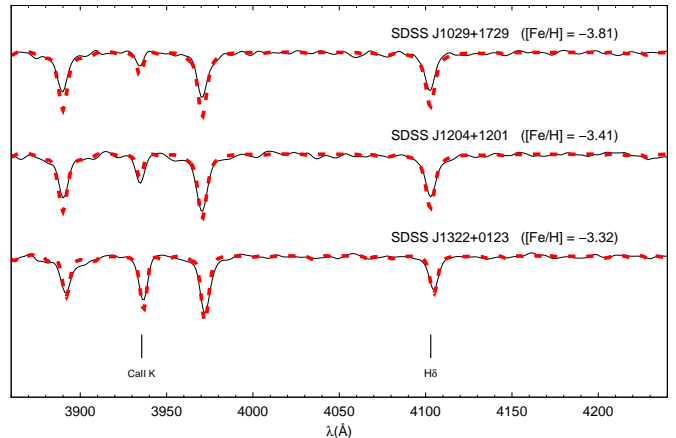


Figure 1. Medium-resolution SDSS/SEGUE spectra for the program stars, compared with SDSS J1029+1729 (top spectrum), a known UMP star from SDSS/SEGUE with $[\text{Fe}/\text{H}] = -4.99$ (Caffau et al. 2011a). The red dashed lines show the synthetic spectra from the SSPP. Also shown are the adopted $[\text{Fe}/\text{H}]$ values from the SSPP.

SDSS J1029+1729 ($[\text{Fe}/\text{H}] = -4.99$ - Caffau et al. 2011a), the first confirmed UMP star from SDSS/SEGUE. The red dashed lines show the SSPP spectral templates, used for matching the observed spectra and to determine the atmospheric parameters. The adopted SSPP metallicities are also shown. It is possible to note a slight mismatch between the observed and synthetic spectra, in particular for $\text{H}\delta$. This results in an overestimated temperature, which translates into a higher $[\text{Fe}/\text{H}]$ value for a given strength of the Ca II K line. By comparing the SSPP parameters with the high-resolution determinations (see Section 3 for details), the SSPP temperatures are overestimated by ~ 400 K, leading to higher estimated $[\text{Fe}/\text{H}]$.

High-resolution data were obtained during the 2013A semester, using the Magellan Inamori Kyocera Echelle (MIKE - Bernstein et al. 2003) spectrograph on the Magellan-Clay Telescope at Las Campanas Observatory. The observing setup included a $0''.7$ slit with 2×2 on-chip binning, which yielded a resolving power of $R \sim 35,000$ in the blue spectral range and $R \sim 28,000$ in the red spectral range. The S/N at 5200 Å is ~ 85 per pixel (using integration times of 60 and 90 minutes for SDSS J1322+0123 and SDSS J1204+1201, respectively). MIKE spectra have nearly full optical wavelength coverage over $\sim 3500 - 9000$ Å. Table 1 lists the details of the high-resolution observations for the program stars. The data were reduced using a data reduction pipeline developed for MIKE spectra, initially described by Kelson (2003)⁹.

Figure 2 shows regions of the MIKE spectra for the program stars in comparison with the EMP star HE 1300+0157, which has similar stellar parameters as our program stars ($T_{\text{eff}} = 5450$ K, $\log g = 3.20$, $[\text{Fe}/\text{H}] = -3.88$; Frebel et al. 2007). The lower left panel shows the region around the Ba II line at 4554 Å; the lower right panel shows the Mg triplet around 5170 Å; and the upper panel shows the Ca II lines.

⁹ <http://code.obs.carnegiescience.edu/python>

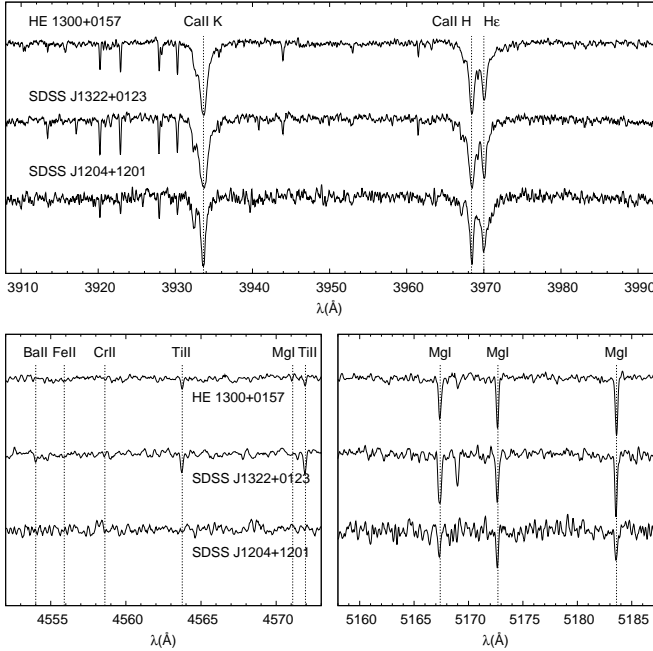


Figure 2. Examples of the spectral regions of our program stars around the Ba II line at 4554 Å, Mg I triplet, and Ca II H and K, compared with the previously studied star HE 1300+0157.

3. STELLAR PARAMETERS AND CHEMICAL ABUNDANCES

3.1. Techniques

Atomic absorption lines were measured using the same line list as in (Frebel et al. 2014), based on lines from Aoki et al. (2002), Barklem et al. (2005), and the VALD database (Kupka et al. 1999). Equivalent-width measurements were obtained by fitting Gaussian profiles to the observed absorption lines. Table 3 lists the lines used in this work, their measured equivalent widths, and the derived abundance from each line.

For the abundance analysis, we employ one-dimensional plane-parallel model atmospheres with no overshooting (Castelli & Kurucz 2004), computed under the assumption of local thermodynamic equilibrium (LTE). The 2011 version of the MOOG synthesis code (Snedden 1973) was used for the spectral synthesis. In this version, scattering is treated with a source function that sums both absorption and scattering components, rather than treating continuous scattering as true absorption (Sobeck et al. 2011).

Elemental abundance ratios, $[X/Fe]$, are calculated taking solar abundances from Asplund et al. (2009). The average measurements (or upper limits) for 16 elements, derived from the MIKE spectra, are listed in Table 4. The σ values are the standard error of the mean. The abundance uncertainties, as well as the systematic uncertainties in the abundance estimates due to the atmospheric parameters, were treated in the same way as described in Placco et al. (2013). For the equivalent-width analysis, any uncertainties calculated to be less than the σ for Fe I was replaced by 0.05 dex. For the spectral synthesis, a best value for the abundance of a given line is assumed, then lower and upper abundance values are set so they enclose the entire spectral feature. That is taken as the uncertainty. For the systematic uncertainties, Ta-

ble 5 shows how changes in each atmospheric parameter affect the determined abundances. Also given is the total uncertainty for each element.

3.2. Stellar Parameters

From the high-resolution MIKE spectra, effective temperatures of the stars were determined by minimizing trends between the abundances derived from Fe I lines and their excitation potentials. The temperatures derived by this procedure are known to be underestimated when compared with T_{eff} based on photometry. As a consequence, such differences also lead to small changes in surface gravities and chemical abundances. Frebel et al. (2013) provide a simple linear relation to correct the spectroscopy-derived “excitation temperatures” to photometric-based temperatures. We apply this procedure and use the corrected T_{eff} to obtain our final stellar parameters. For warmer stars on the subgiant branch and near the main-sequence turnoff, these corrections are fortunately small. In our cases, the temperature corrections were 137 K for SDSS J1322+0123, and 188 K for SDSS J1204+1201. Microturbulent velocities were determined by minimizing the trend between the abundances of Fe I lines and their reduced equivalent widths.

For SDSS J1322+0123, the surface gravity was determined from the balance of two ionization stages for iron lines (Fe I and Fe II). We allowed the difference between the abundances of the Fe I and Fe II lines to be 0.02 dex. For SDSS J1204+1201, since no Fe II lines could be measured, the surface gravity was estimated from a Yale-Yonsei isochrone (Demarque et al. 2004) with 12 Gyr, $[Fe/H] = -3.5$, and $[\alpha/Fe] = +0.4$. The final atmospheric parameters for the program stars are listed in Table 2.

3.3. Abundances and Upper Limits

3.3.1. Lithium

We were able to determine the LTE lithium abundance for SDSS J1204+1201. From the doublet at 6707.8 Å, the spectral synthesis resulted in $A(\text{Li}) = 1.70^{10}$. Lind et al. (2009) provide NLTE corrections for Li abundances, based on evolutionary status and $A(\text{Li})$. From their Figures 1-3, it is possible to see that the corrections (for $T_{\text{eff}} = 6000$ K and $A(\text{Li}) = 1.70$) are less than 0.05 dex, which is within the uncertainty of the observed abundances for SDSS J1204+1201.

Figure 3 shows the spectral synthesis for the Li line in SDSS J1204+1201. The dots represent the observed spectrum, and the solid line is the best abundance fit. The shaded area encompasses a ± 0.3 dex difference in $A(\text{Li})$. The synthesized spectrum without Li is represented by the light gray line.

3.3.2. Carbon

It was possible to measure the carbon abundance for SDSS J1322+0123 ($[C/Fe] = +0.49$), using the CH G-band region around 4300 Å. For SDSS J1204+1201, an upper limit was determined ($[C/Fe] < +1.45$), using the procedure described in Frebel et al. (2006). Figure 4 shows the CH G-band spectral synthesis for SDSS J1322+0123. The large black dots represent the

¹⁰ Here we employ the notation $A(X) = \log \epsilon(X) + 12.0$

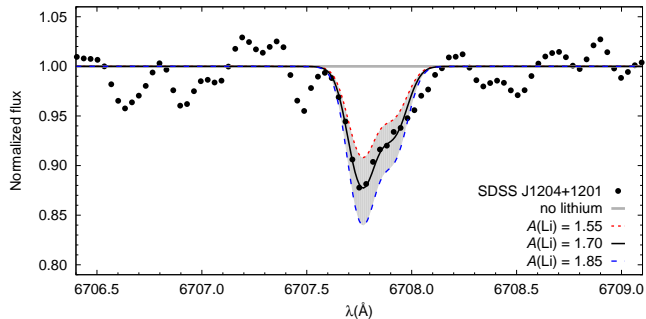


Figure 3. Li abundance determination for SDSS J1204+1201. The dots represent the observed spectrum, the solid line is the best abundance fit, and the dotted and dashed lines indicate the abundance uncertainty. The shaded area encompasses a ± 0.3 dex difference in $A(\text{Li})$. The light gray line shows the synthesized spectrum in the absence of any Li.

observed spectrum, and the solid line is the best abundance fit. The dotted and dashed line represent a ± 0.2 dex variation in $[\text{C}/\text{Fe}]$, which we conservatively use as the uncertainty. We also calculated the carbon abundance corrections for SDSS J1322+0123, based on the procedure described by Placco et al. (2014b). For $\log g = 1.95$, $[\text{Fe}/\text{H}] = -3.64$, and $[\text{C}/\text{Fe}] = +0.49$, the correction is 0.01 dex for the $[\text{N}/\text{Fe}] = 0.0$ case.

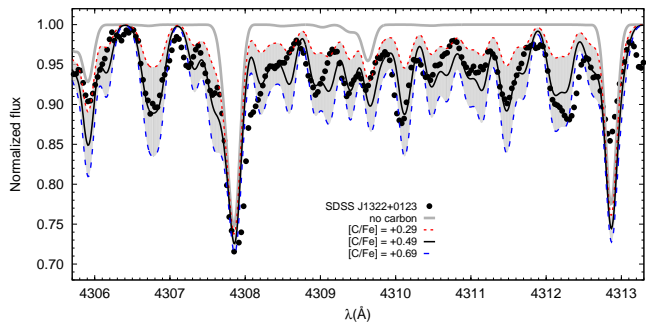


Figure 4. Carbon abundance estimate for SDSS J1322+0123. The large black dots represent the observed spectrum, the solid line is the best abundance fit, and the dotted and dashed lines indicate the abundance uncertainty. The shaded area encompasses a ± 0.2 dex difference in $[\text{C}/\text{Fe}]$. The light gray line shows the synthesized spectrum in the absence of any carbon.

3.3.3. From Na to Ni

For the elements Na, Mg, Al, Si, Ca, Sc, Ti, Cr, Mn, Co, and Ni, abundances were determined from equivalent-width analysis only. For SDSS J1322+0123, no particular discrepancies were found for elements with abundances determined for more than one line. The standard errors of the average abundances are typically smaller than 0.10 dex. In the case of SDSS J1204+1201, only Na and Mg (besides Fe) have more than one measured line, both with $\sigma = 0.05$ dex.

3.3.4. Neutron-capture Elements

For SDSS J1322+0123, neutron-capture element abundances were determined from spectral synthesis. For Sr II, the lines used were 4077 Å ($[\text{Sr}/\text{Fe}] = -1.29$) and 4215 Å ($[\text{Sr}/\text{Fe}] = -1.20$); the Ba II abundance was measured from the 4554 Å ($[\text{Ba}/\text{Fe}] = -1.30$) line. Figure 5

shows the comparison between the observed and synthetic spectra for these three lines in SDSS J1322+0123. There is good agreement between the abundances of the two Sr lines (values within 0.1 dex). Only upper limits were determined for SDSS J1204+1201 ($[\text{Sr}/\text{Fe}] < -0.08$ and $[\text{Ba}/\text{Fe}] < +0.62$).

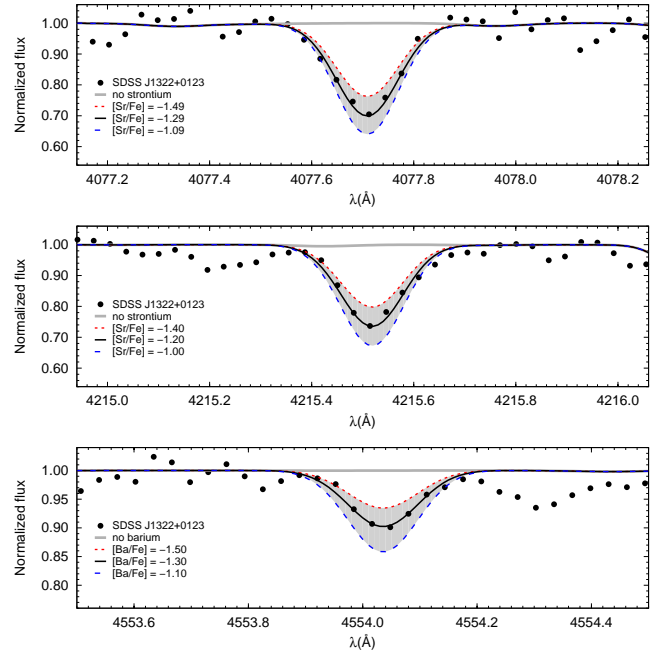


Figure 5. Sr and Ba abundance determinations for SDSS J1322+0123. The dots represent the observed spectrum, the solid line is the best abundance fit, and the dotted and dashed lines indicate the abundance uncertainty. The shaded area encompasses a ± 0.2 dex difference in $\log \epsilon$ (Sr) and $\log \epsilon$ (Ba) abundances. The light gray line shows the synthesized spectrum in the absence of any Sr and Ba, respectively.

4. DISCUSSION

There are many reasons why observations of new stars in the metallicity range $[\text{Fe}/\text{H}] < -3.5$ are important. These include a proper description of the low-metallicity tail of the Galactic Halo MDF, as well as the nature of the progenitor populations of UMP stars. Below we show a comparison between the abundances of the program stars and other stellar abundances from the literature, as well as an attempt to describe the main characteristics (e.g., mass and explosion energy) of UMP star progenitors.

4.1. Comparison with Literature Abundance Trends

4.1.1. Lithium

SDSS J1204+1201 is a subgiant ($\log(L/L_\odot) = 1.04$, assuming $M = 0.8 M_\odot$), and has $A(\text{Li}) = 1.7$, well below the Li plateau for metal-poor dwarf stars described by Spite & Spite (1982). Figure 6 shows the behavior of Li abundances, as a function of temperature, for a sample of metal-poor stars from the literature. Individual references are listed in the figure caption. The Li $A(\text{Li}) = 1.7$ abundance for SDSS J1204+1201 is consistent with data from the literature at the same temperature and metallicity, and suggests that Li is already being depleting on the lower giant branch, due, at least in part, to internal processing.

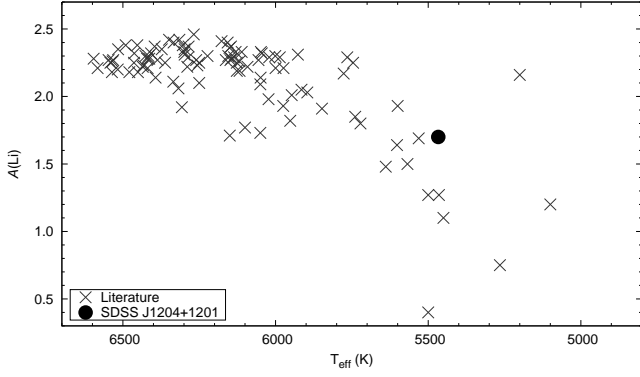


Figure 6. $A(\text{Li})$ vs. T_{eff} for SDSS J1204+1201, compared to literature data. References include Frebel et al. (2007); Meléndez et al. (2010); Masseron et al. (2012); Hansen et al. (2014, 2015).

4.1.2. Other Elements

We also compared the abundances of our sample stars with the EMP star samples from Yong et al. (2013a) (giants only) and Hansen et al. (2014). Results are shown in Figure 7. The carbon abundances from the literature were also corrected using the procedure described in Placco et al. (2014b). No significant differences are found for the light elements, except for Al, which falls below the trend for the literature data. The upper limits of C, Sr, and Ba for SDSS J1204+1201 are also consistent with typical values for halo stars in this metallicity range.

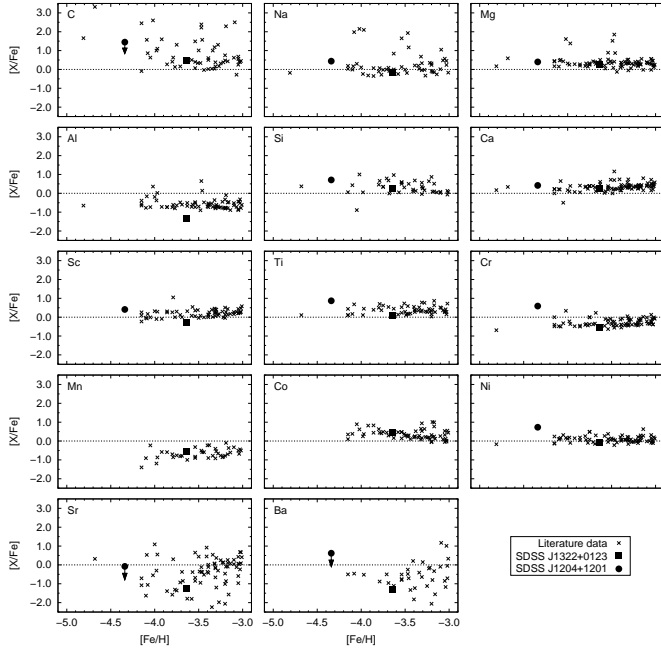


Figure 7. $[X/\text{Fe}]$ vs. $[\text{Fe}/\text{H}]$ for carbon, α -, iron-peak, and neutron-capture elements, for the program stars and stars with $[\text{Fe}/\text{H}] < -3.0$ from Yong et al. (2013a) and Hansen et al. (2014).

SDSS J1322+0123 is moderately enhanced in carbon ($[\text{C}/\text{Fe}] = +0.49$). Given its high gravity, the carbon correction is only 0.01 dex, leading to $[\text{C}/\text{Fe}]_c = +0.50$. Even though in the $[\text{Fe}/\text{H}] < -3.5$ metallicity range, 70 % of the stars exhibit $[\text{C}/\text{Fe}] > +0.50$ (Placco et al.

2014b), the carbon abundance of SDSS J1322+0123 appears to be within expectations. For SDSS J1204+1201, the $[\text{C}/\text{Fe}] < +1.45$ is also within expectations, given that 80 % of the stars with $[\text{Fe}/\text{H}] < -4.3$ show $[\text{C}/\text{Fe}] > +1.0$. However, a higher S/N spectrum is needed for a proper carbon abundance determination for SDSS J1204+1201. The abundances of Ti, Cr, and Ni for SDSS J1204+1201 appear to be higher than the trends presented by the literature data. We caution the reader, however, that the abundances for these species were derived by equivalent-width analysis of only one spectral feature. Further measurements are needed to properly address this issue.

In the $[\text{Fe}/\text{H}] < -3.0$ regime, the neutron-capture elements Sr and Ba are thought to be formed by the r -process, rather than the s -process, which dominates at $[\text{Fe}/\text{H}] > -2.5$ (Placco et al. 2013). The low values determined for SDSS J1322+0123 are consistent with the literature data. The $[\text{Sr}/\text{Ba}] = +0.06$ value is also within the range for stars with $[\text{Fe}/\text{H}] < -3.5$ (Aoki et al. 2013).

4.2. Model Predictions for UMP Progenitors

In this section we attempt to assess the properties (mass distribution and explosion energies) of the progenitor population of UMP stars. For this exercise, we used SDSS J1204+1201 and 19 UMP stars with parameters and abundances determined from high-resolution spectroscopy, gathered by Placco et al. (2014b). Individual references and parameters are listed in Table 6. The abundance data were compared to the theoretical model predictions for non-rotating single massive Population III stars, in the range $10 M_{\odot} - 100 M_{\odot}$ of Heger & Woosley (2010). The model database comprises 120 initial masses, and explores a range of explosion energies from 0.3×10^{51} erg to 10×10^{51} erg kinetic energy of the ejecta. The models further vary the amount of mixing in the supernova ejecta due to Rayleigh Taylor instabilities (e.g., Joggerst et al. 2009). Here we also use their χ^2 matching algorithm (Heger & Woosley 2010). An on-line tool including the model database can be found at `starfit`¹¹. The same fitting procedure was also used in Keller et al. (2014), Bessell et al. (2015), and Frebel et al. (2015). In this work we adopt a similar procedure as the one described in Heger & Woosley (2010), using all available element measurements and upper limits up to atomic number $Z = 30$. For Cr and Sc, the authors assumed that there are additional production sites not included in the model data, e.g., contributions from neutron star winds, and hence the model yield was taken as lower limit.

4.2.1. Best Model Fits

Chemical abundances (and/or upper limits) for the UMP sample are available for the following species: C, N, O, Na, Mg, Al, Si, Ca, Sc, Ti, V, Cr, Mn, Fe, Co, Ni, and Zn. For the solar abundances, the `starfit` code uses the photospheric values from Asplund et al. (2009).

Figures 8 and 9 show the best model fit for the 21 UMP stars in Table 6. The red filled squares represent all the abundances gathered from the individual studies (including upper limits as arrows). The solid black line

¹¹ <http://starfit.org>

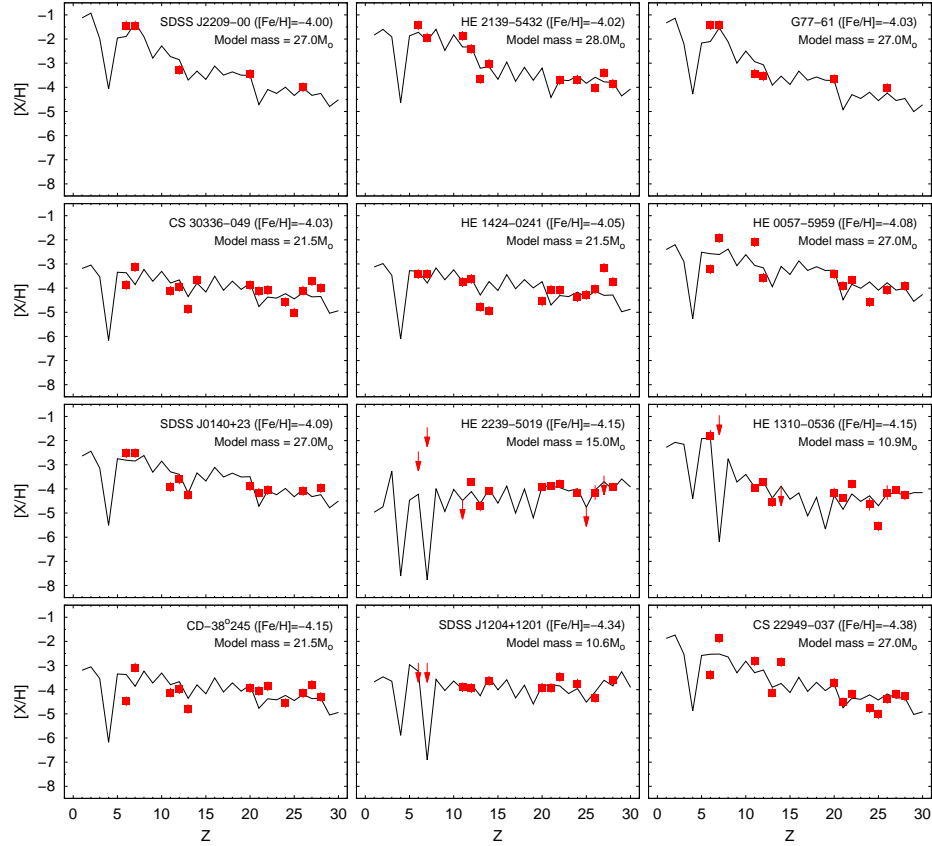


Figure 8. Abundance ratios $[X/H]$ as a function of charge number Z for the first twelve UMP stars. *Red filled squares* are abundances taken from the literature (see text for comments on carbon and nitrogen). The *solid line* is the best fit for each star, with the model mass shown in the upper right. *Arrows* represent upper limits.

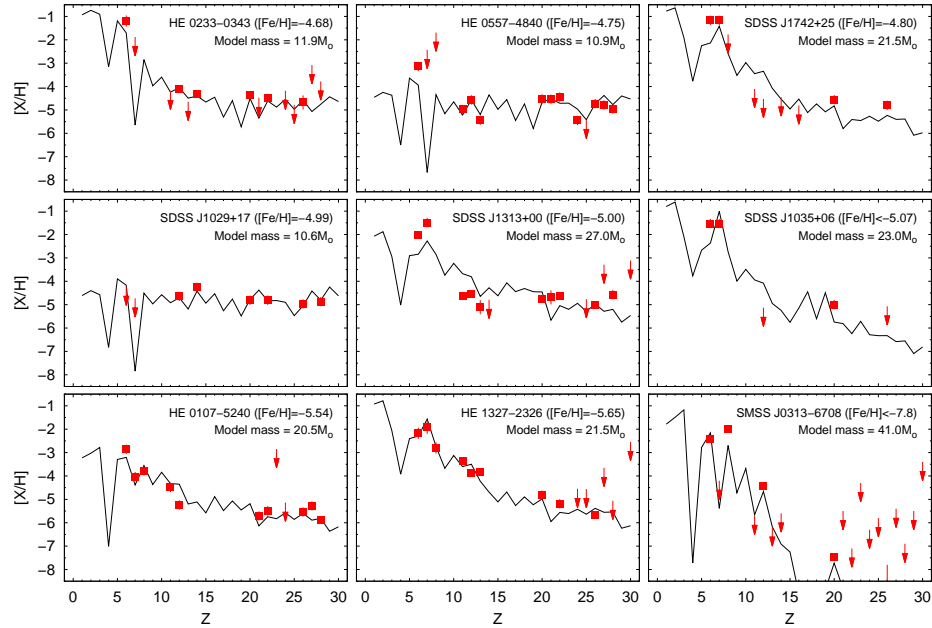


Figure 9. Abundance ratios $[X/H]$ as a function of charge number Z for the second nine UMP stars. *Red filled squares* are abundances taken from the literature (see text for comments on carbon and nitrogen). The *solid line* is the best fit for each star, with the model mass shown in the upper right. *Arrows* represent upper limits.

is the best model fit to the data. Among the 21 stars, six do not have nitrogen abundance measurements or upper limits. For those, we estimated the nitrogen abundance using $[C/N] = 0.0$ (see discussion below and top panel of

Figure 11 in Placco et al. 2014b). For the carbon abundances, seven stars had their abundances corrected for their evolutionary status using the procedures described in Placco et al. (2014b). A summary of the abundances

and corrections applied to the data is shown in Table 6.

From the figures, one can see no relation between the progenitor mass and the iron abundance of the UMP stars. This may be expected, since the $[\text{Fe}/\text{H}] < -4.0$ range is believed to probe second-generation stars, for which the local enrichment from the Pop III star explosion is expected to dominate over global chemical evolution effects. In addition, it is possible to see that the models always predict a very low nitrogen abundance ($[\text{N}/\text{H}] < -6.0$) where only upper limits on nitrogen are determined. This has a direct impact on the best model chosen by the `starfit` code, and introduces an artifact on the progenitor mass distribution, as explained below. Also, for stars where $[\text{N}/\text{H}]$ is higher than $[\text{C}/\text{H}]$ by more than 1.0 dex (e.g. HE 0057–5959, CD–38°245, and CS 22949–037), the model is not capable of reproducing the CN pattern, and the overall fit yields a higher residual value.

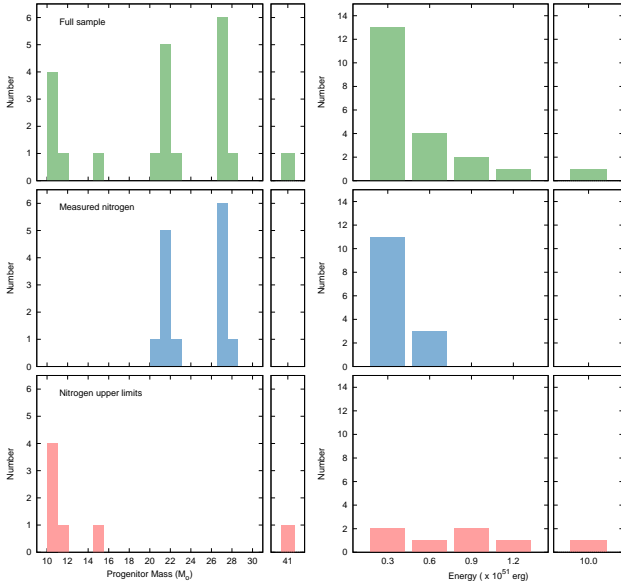


Figure 10. Progenitor mass (left panels) and explosion energy (right panels) distributions for the best model fits for the 18 UMP stars. Upper panels: full sample. Middle panels: stars with measured nitrogen abundances. Bottom panels: stars with nitrogen upper limits.

Figure 10 shows the progenitor mass (left panels) and explosion energy (right panels) distributions for the best model fits. The upper panels show the full sample (21 stars), the middle panels show stars with measured nitrogen abundances (14 stars – including the estimates from Table 6), and the bottom panels show stars with nitrogen upper limits (seven stars). For the progenitor mass, a clear separation in the distributions is seen in the middle and bottom panels. Progenitor masses for stars with upper limits on nitrogen concentrate in the $10.6 - 15.0 M_{\odot}$ range. In contrast, progenitor masses for stars with measured nitrogen abundance show two preferred ranges: $20.5 - 23.0 M_{\odot}$ and $27.0 - 28.0 M_{\odot}$. Concerning the explosion energy, more than 75 % of the stars with measured nitrogen show 0.3×10^{51} erg, regardless of the progenitor mass ranges listed above. This can either be an indication of the nature of these progenitors, or an numerical artifact, since this is the lowest available energy within the model grid. In one particular case

(HE 2239–5019), the explosion energy is the maximum value allowed by the models (10×10^{51} erg). This spurious result could be explained by the lack of carbon and nitrogen abundance measurements (see explanation below in Sections 4.2.2 and 4.2.3.), or by the behavior of the abundance pattern for the light elements.

For the stars with measured nitrogen, interesting differences in the progenitor population arise for the lowest metallicity stars in the sample; one example is the difference in the CNO pattern of HE 0107–5240 and HE 1327–2326. Even though these two stars have $[\text{Fe}/\text{H}]$ values within 0.2 dex of one another, and estimated progenitor masses within 5 %, HE 1327–2326 has a $\log \epsilon(\text{N})$ two orders of magnitude higher than HE 0107–5240. In the context of this work, this difference could be explained by changes in mass and explosion energy (0.6×10^{51} erg for HE 0107–5240 and 0.3×10^{51} erg for HE 1327–2326), and does not require additional models to describe the progenitor population. Another less extreme comparison is for CS 30336–049 and HE 1424–0241: their metallicity, carbon, and nitrogen abundances are within 0.02 dex, 0.16 dex, and 0.29 dex, respectively, and both share the same best model fit ($21.5 M_{\odot}$ and 0.3×10^{51} erg). For SDSS J1742+25 ($[\text{Fe}/\text{H}] < -5.07$), even though the progenitor mass and explosion energy ($23.0 M_{\odot}$ and 0.6×10^{51} erg) are similar to other stars in the same $[\text{Fe}/\text{H}]$ range, the small number of determined abundances (C and Ca) clearly affects the fitting procedure (see discussion below). Additional abundance measurements for these stars, as well as the discovery of more stars in this $[\text{Fe}/\text{H}]$ range are needed for further investigation. For the most iron-poor star known, SMSS J0313–6708, even though our results are consistent with the models described in (Bessell et al. 2015), the lack of nitrogen abundance measurement is possibly affecting the progenitor mass determination.

4.2.2. Robustness of Best Model Fits

The `starfit` procedure gives the ten best model fits for a given set of input abundances, ranked by their χ^2 value. To test the robustness of the best solution, we analyzed the χ^2 variation between the ten best models for each star, and how they affect the progenitor mass. For instance, a flat χ^2 distribution with a wide range of progenitor masses is an indication that the solutions are not very robust. Ideally, the χ^2 value should rapidly increase between the first and second-best solutions.

Figure 11 shows the evolution of the χ^2 values as a function of the model rank. Each line represents a star on Table 6, labeled by its “Star ID”. The numbers above each point are the variations (in %) of the χ^2 value for a given model, compared to the χ^2 value of the best model fit. The point size is proportional to the progenitor mass, with approximate values labeled on the top left. Inspection of Figure 11 reveals that, for 2/3 of the sample stars, the variation in χ^2 between the first and second-best models is above 10 %. In addition, for six out of eight stars where the χ^2 variation is below 10 %, the progenitor masses only changes in two cases. For these stars – #6 (HE 0057–5959) and #10 (CD–38°245) – the variation is between $21.5 M_{\odot}$ and $27.0 M_{\odot}$, which are precisely the two preferred mass values according to Figure 10 (see discussion above). For stars #4 (CS 30336–049) and #5

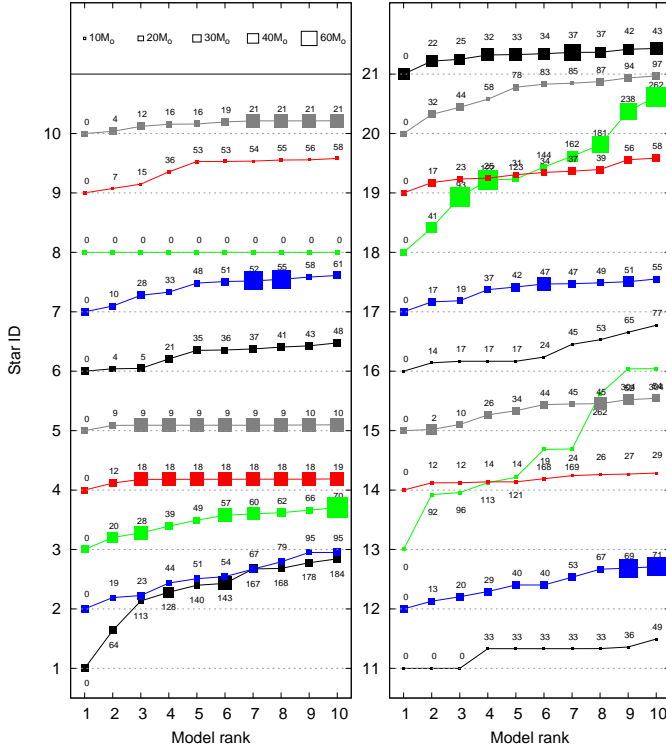


Figure 11. Change (in χ^2 %) on the residual values as a function of the model rank for the sample stars. The y-axis shows the Star ID from Table 6. The point size is proportional to the progenitor mass for each model.

(HE 1424–0241), there is a large change in mass between model-rank 2 and 3, with a small variation in χ^2 . Even though both stars have 14 determined abundances, additional work must be performed to evaluate whether the measurements or the models could be changed to generate a better agreement. For stars #15 (SDSS J1742+25) and #18 (SDSS J1035+06), the low number of determined abundances compromises the robustness of the best model fits.

4.2.3. Uncertainty/Robustness in the Progenitor Mass

Chemical abundance measurements carry uncertainties related to the choice of model atmosphere, continuum placement when measuring absorption line strengths, and atomic data line lists. In addition, non-LTE and 3D effects also have an impact on the determinations. All of these changes in the abundances can generate changes in the progenitor-star properties. Keeping the observed uncertainty in mind, we are using C and N as representative examples, as the fitting results appear to most strongly depend on them. As shown above, the existence of a nitrogen measurement is quite important for the model-fit procedure.

The stellar evolution of primordial stars, which are the basis of this study, is very peculiar. These primordial stars have no initial CNO, so in order to burn hydrogen – for which they need the CNO cycle – they need to produce a trace of CNO material themselves. Typical mass fractions are 10^{-7} or less at the end of core hydrogen burning and in the H-burning shell. Because of that, any significant amounts of nitrogen found in the UMP stars (and not made by them *in situ*) must come from

another primordial production mechanism in the Pop III stars, during or after the onset of central helium burning, and by mixing of the He burning products with the H envelope. Without rotation or other mixing processes, in the models of Heger & Woosley (2010) this only occurred consistently for initial masses of $45 M_{\odot}$ and above (their Figure 11), whereas most of the lower-mass models did not have large nitrogen yields. Hence observational constraints from nitrogen measurements or upper limits can significantly constrain the mass range of models that provide a good fit.

In order to evaluate how changes in the nitrogen (and/or carbon) abundance reflect on the progenitor mass, we ran the `starfit` procedure for the 21 UMP stars for ten different scenarios, listed in Table 7. Then, we evaluated how the progenitor mass of the best model changes. Figure 12 shows how the progenitor mass changes for each star, for the ten cases listed in Table 7, compared with the result of the best-fit model presented in Figures 8 and 9, and Table 6. Blue filled dots are stars with available carbon and nitrogen measurements, and red filled dots represent stars with available upper limits for carbon and/or nitrogen.

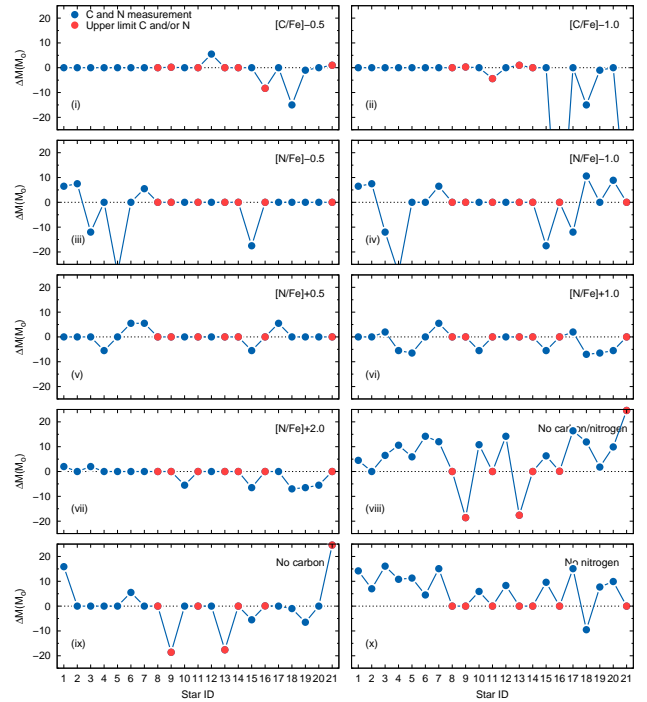


Figure 12. Variations (in M_{\odot}) in the progenitor mass (compared to that of the best-fit model) for the sample stars, for the ten cases described above. Blue filled dots are stars with available carbon and nitrogen abundance measurements, and red filled dots are stars with upper limits for carbon and/or nitrogen.

When changing the carbon abundances – cases (i) and (ii) – the stars affected with available carbon and/or nitrogen measurements are #12 (CS 22949–037), and #18 (SDSS J1035+0641). Star #12 has its progenitor mass changed from $27.0 M_{\odot}$ to $21.5 M_{\odot}$ (within the mass range shown in the middle panels of Figure 10), and star #18 from $23.0 M_{\odot}$ to $38.0 M_{\odot}$. The latter case has only three determined abundances, which makes the model-fitting more susceptible to changes. For nitrogen, large

changes in progenitor mass are seen (for stars #1, #2, #3, #4, #5, #7, and #15) when reducing the $[\text{N}/\text{Fe}]$ abundances – cases (iii) and (iv). For positive changes in nitrogen – cases (v), (vi), and (vii) – there are smaller progenitor masses variations for a handful of stars. These variations, however, are always between $20\text{ M}_{\odot} - 22\text{ M}_{\odot}$ and $27\text{ M}_{\odot} - 29\text{ M}_{\odot}$, agreeing with the two distributions shown in the middle panel of Figure 10.

When removing the carbon abundances from the fit – case (ix) – the only considerable change (apart from the stars with upper limits) is for star #1 (SDSS J2209–0028). This can be explained by the low number of abundances – five – used for the fit. The most noticeable changes happen for cases (viii) and (x), when the nitrogen abundance is removed. Then, every progenitor mass is changed by at least 5 M_{\odot} .

With these tests, we show that the models are sufficiently robust to not be affected by typical uncertainties in $[\text{C}/\text{Fe}]$ and $[\text{N}/\text{Fe}]$ (< 0.3 dex). Moreover, regardless of the number of abundances available for the fit, we stress the strong effect the presence (or absence) of nitrogen abundances has on the final result. Below we compare our results with a similar study, in which abundance patterns of stars with $[\text{Fe}/\text{H}] < -3.5$ are compared with a set of SN models with fixed masses.

4.2.4. Comparison with Tominaga et al. (2014) Results

Tominaga et al. (2014) performed abundance profiling for 48 stars with $[\text{Fe}/\text{H}] < -3.5$ from the literature, to gain insight into the properties of the Pop III progenitors. The authors use Pop III SN models with 25 M_{\odot} and 40 M_{\odot} . With the fixed mass, free parameters are explosion energy, remnant mass, and ejected mass. They also include models with 25 M_{\odot} and enhanced mixing due to rapid rotation.

There are ten stars in common between Tominaga et al. (2014) and this work. For all these stars, the explosion energy of their 25 M_{\odot} SN progenitor is higher (by at least an order of magnitude) than the values found by this work. Regardless, it is interesting to see that the progenitor mass range found by the `starfit` ($20.5\text{ M}_{\odot} - 28.0\text{ M}_{\odot}$ – when using both C and N for the matching) is consistent with a 25 M_{\odot} progenitor. For the two most iron-poor stars analyzed by Tominaga et al. (2014) – HE 0107–2326 and HE 1327–2326 – the authors find similar explosion energies and remnant masses for both stars, regardless of the different nitrogen abundances. In their Figure 7, however, the models cannot properly reproduce the nitrogen abundance for HE 1327–2326.

Ishigaki et al. (2014) also performs abundance profiling for stars with $[\text{Fe}/\text{H}] < -4.5$. Their best-fit models for HE 0107–2326, HE 1327–2326, and HE 0557–4840 (high carbon abundances) have 25 M_{\odot} and explosion energy of 1.0×10^{51} erg. Similar to what was found by Tominaga et al. (2014), the high N abundance for HE 1327–2326 is also not reproduced, with the models consistently underproducing nitrogen when compared to the observed values, by at least 2 dex. For SDSS J1029+1729, the authors find a suitable model with 40 M_{\odot} and explosion energy of 30.0×10^{51} erg.

An alternative formation scenario for this star, which includes dust-induced cooling, is given by Schneider et al. (2012), where the authors find good agreement between observations and the yields of core-collapse SNe

with metal-free progenitors of 20 M_{\odot} and 35 M_{\odot} . In the case of SMSS J0313–6708, models with 25 M_{\odot} and 40 M_{\odot} well-reproduce the abundances of carbon, magnesium, and calcium, as well as the upper limit for nitrogen. In contrast, the model presented in this work for SMSS J0313–6708 also has a good overall abundance fit, even though it has a higher mass (60 M_{\odot}) and lower explosion energy – 1.0×10^{51} erg as opposed to 10.0×10^{51} erg.

5. CONCLUSIONS

In this work we presented the high-resolution abundance analysis of two stars selected from the SDSS/SEGUE survey, with $[\text{Fe}/\text{H}] = -3.64$ and $[\text{Fe}/\text{H}] = -4.34$. A detailed chemical abundance analysis reveals that these stars show the expected behavior of stars in the same metallicity range. The addition of these two stars to the $[\text{Fe}/\text{H}] < -3.5$ range corroborates with the hypothesis presented by Yong et al. (2013b) that the Galactic Halo MDF smoothly decreases down to $[\text{Fe}/\text{H}] = -4.1$, instead of the sharp cutoff at $[\text{Fe}/\text{H}] = -3.6$ suggested by Schörck et al. (2009) and Li et al. (2010).

We also provide new insights on the progenitor population of UMP stars, by comparing their abundance patterns to a set of theoretical SN models. We find that all UMP stars with carbon and nitrogen abundances available have progenitors with masses in either $20.5\text{ M}_{\odot} - 23.0\text{ M}_{\odot}$ or $27.0\text{ M}_{\odot} - 28.0\text{ M}_{\odot}$ ranges, with explosion energies between 0.3 and 0.9×10^{51} erg. We stress that, even though there could be additional suitable candidates for the UMP progenitors, such as the fast rotating massive stars from Meynet et al. (2006) and the faint supernovae from Tominaga et al. (2014), the models presented in this work are capable of describing the differences in the abundance patterns by adjusting the progenitor mass and explosion energy.

Comparison with similar studies from the literature shows that, even though higher progenitor masses ($M = 40\text{ M}_{\odot}$) also show good agreement for the most extreme cases, such as SMSS J0313–6708, models have their best fits for 25 M_{\odot} , which is consistent with the mass range found in this work. Besides having additional targets at $[\text{Fe}/\text{H}] < -4.0$ for comparison, it is important to have accurate nitrogen and light element abundances for all UMP stars in the literature. There are still a number of similar candidates in need of high-resolution follow-up, and we expect to conduct similar studies in the near future.

V.M.P. and T.C.B. acknowledge partial support for this work from grants PHY 08-22648; Physics Frontier Center/Joint Institute of Nuclear Astrophysics (JINA), and PHY 14-30152; Physics Frontier Center/JINA Center for the Evolution of the Elements (JINA-CEE), awarded by the US National Science Foundation. A.F. is supported by NSF CAREER grant AST-1255160. Y.S.L. acknowledges partial support by the 2014 research fund of Chungnam National University and support from the National Research Foundation of Korea to the Center for Galaxy Evolution Research. A.H. was supported by a Future Fellowship of the Australian Research Council (FT120100363).

REFERENCES

- Allen, D. M., Ryan, S. G., Rossi, S., Beers, T. C., & Tsangarides, S. A. 2012, *A&A*, 548, A34
- Allende Prieto, C., Sivarani, T., Beers, T. C., et al. 2008, *AJ*, 136, 2070
- Allende Prieto, C., Fernandez-Alvar, E., Aguado, D. S., et al. 2015, arXiv:1505.05555
- Aoki, W., Ryan, S. G., Norris, J. E., et al. 2002, *ApJ*, 580, 1149
- Aoki, W., Beers, T. C., Lee, Y. S., et al. 2013, *AJ*, 145, 13
- Asplund, M., Grevesse, N., Sauval, A. J., & Scott, P. 2009, *ARA&A*, 47, 481
- Barklem, P. S., Christlieb, N., Beers, T. C., et al. 2005, *A&A*, 439, 129
- Beers, T. C., & Christlieb, N. 2005, *ARA&A*, 43, 531
- Beers, T. C., Preston, G. W., & Shectman, S. A. 1985, *AJ*, 90, 2089
- . 1992, *AJ*, 103, 1987
- Bernstein, R., Shectman, S. A., Gunnels, S. M., Mochnacki, S., & Athey, A. E. 2003, in *Society of Photo-Optical Instrumentation Engineers (SPIE) Conference Series*, Vol. 4841, Society of Photo-Optical Instrumentation Engineers (SPIE) Conference Series, ed. M. Iye & A. F. M. Moorwood, 1694
- Bessell, M., Collett, R., Keller, S., et al. 2015, *ArXiv e-prints*, arXiv:1505.03756
- Bonifacio, P., Sbordone, L., Caffau, E., et al. 2012, *A&A*, 542, A87
- Bonifacio, P., Caffau, E., Spite, M., et al. 2015, *ArXiv e-prints*, arXiv:1504.05963
- Caffau, E., Bonifacio, P., François, P., et al. 2011a, *Nature*, 477, 67
- . 2011b, *A&A*, 534, A4
- Castelli, F., & Kurucz, R. L. 2004, *ArXiv Astrophysics e-prints*, arXiv:astro-ph/0405087
- Christlieb, N., Schörck, T., Frebel, A., et al. 2008, *A&A*, 484, 721
- Christlieb, N., Bessell, M. S., Beers, T. C., et al. 2002, *Nature*, 419, 904
- Demarque, P., Woo, J.-H., Kim, Y.-C., & Yi, S. K. 2004, *ApJS*, 155, 667
- Frebel, A., Chiti, A., Ji, A. P., Jacobson, H. R., & Placco, V. M. 2015, *ArXiv e-prints*, arXiv:1507.01973
- Frebel, A., Casey, A. R., Jacobson, H. R., & Yu, Q. 2013, *ApJ*, 769, 57
- Frebel, A., & Norris, J. E. 2013, *Metal-Poor Stars and the Chemical Enrichment of the Universe* (Published), 55
- Frebel, A., Norris, J. E., Aoki, W., et al. 2007, *ApJ*, 658, 534
- Frebel, A., Simon, J. D., & Kirby, E. N. 2014, *ApJ*, 786, 74
- Frebel, A., Aoki, W., Christlieb, N., et al. 2005, *Nature*, 434, 871
- Frebel, A., Christlieb, N., Norris, J. E., et al. 2006, *ApJ*, 652, 1585
- Hansen, T., Hansen, C. J., Christlieb, N., et al. 2014, *ApJ*, 787, 162
- . 2015, *ArXiv e-prints*, arXiv:1506.00579
- Heger, A., & Woosley, S. E. 2002, *ApJ*, 567, 532
- . 2010, *ApJ*, 724, 341
- Ishigaki, M. N., Tominaga, N., Kobayashi, C., & Nomoto, K. 2014, *ApJ*, 792, L32
- Iwamoto, N., Umeda, H., Tominaga, N., Nomoto, K., & Maeda, K. 2005, *Science*, 309, 451
- Joggerst, C. C., Woosley, S. E., & Heger, A. 2009, *ApJ*, 693, 1780
- Keller, S. C., Bessell, M. S., Frebel, A., et al. 2014, *Nature*, 506, 463
- Kelson, D. D. 2003, *PASP*, 115, 688
- Kupka, F., Piskunov, N., Ryabchikova, T. A., Stempels, H. C., & Weiss, W. W. 1999, *A&AS*, 138, 119
- Lee, Y. S., Beers, T. C., Sivarani, T., et al. 2008a, *AJ*, 136, 2022
- . 2008b, *AJ*, 136, 2050
- Lee, Y. S., Beers, T. C., Allende Prieto, C., et al. 2011, *AJ*, 141, 90
- Lee, Y. S., Beers, T. C., Masseron, T., et al. 2013, *AJ*, 146, 132
- Li, H. N., Christlieb, N., Schörck, T., et al. 2010, *A&A*, 521, 10
- Lind, K., Asplund, M., & Barklem, P. S. 2009, *A&A*, 503, 541
- Masseron, T., Johnson, J. A., Lucatello, S., et al. 2012, *ApJ*, 751, 14
- Meléndez, J., Casagrande, L., Ramírez, I., Asplund, M., & Schuster, W. J. 2010, *A&A*, 515, L3
- Meynet, G., Ekström, S., & Maeder, A. 2006, *A&A*, 447, 623
- Meynet, G., Hirschi, R., Ekström, S., et al. 2010, *A&A*, 521, A30
- Nomoto, K., Kobayashi, C., & Tominaga, N. 2013, *ARA&A*, 51, 457
- Nomoto, K., Tominaga, N., Umeda, H., Kobayashi, C., & Maeda, K. 2006, *Nuclear Physics A*, 777, 424
- Placco, V. M., Frebel, A., Beers, T. C., et al. 2014a, *ApJ*, 781, 40
- . 2013, *ApJ*, 770, 104
- Placco, V. M., Frebel, A., Beers, T. C., & Stancliffe, R. J. 2014b, *ApJ*, 797, 21
- Rockosi, C., others, others, et al. 2015, *ApJ*, in preparation
- Roederer, I. U. 2013, *AJ*, 145, 26
- Schneider, R., Omukai, K., Limongi, M., et al. 2012, *MNRAS*, 423, L60
- Schörck, T., Christlieb, N., Cohen, J. G., et al. 2009, *A&A*, 507, 817
- Smolinski, J. P., Lee, Y. S., Beers, T. C., et al. 2011, *AJ*, 141, 89
- Snedden, C. A. 1973, PhD thesis, The University of Texas at Austin.
- Sobeck, J. S., Kraft, R. P., Sneden, C., et al. 2011, *AJ*, 141, 175
- Spite, F., & Spite, M. 1982, *A&A*, 115, 357
- Spite, M., Caffau, E., Bonifacio, P., et al. 2013, *A&A*, 552, A107
- Tominaga, N., Iwamoto, N., & Nomoto, K. 2014, *ApJ*, 785, 98
- Yanny, B., Rockosi, C., Newberg, H. J., et al. 2009, *AJ*, 137, 4377
- Yong, D., Norris, J. E., Bessell, M. S., et al. 2013a, *ApJ*, 762, 26
- . 2013b, *ApJ*, 762, 27
- York, D. G., Adelman, J., Anderson, Jr., J. E., et al. 2000, *AJ*, 120, 1579

Table 1
Observational Data

	SDSS J1322+0123 ^a	SDSS J1204+1201 ^b
α (J2000)	13:22:50.6	12:04:41.4
δ (J2000)	+01:23:43.0	+12:01:11.5
g (mag)	16.3	16.4
$g-r$	0.50	0.34
High Resolution – Magellan/MIKE		
Date	2013 05 30	2013 05 31
UT	02:35:55	00:09:39
Exptime (s)	3600	5400
v_r (km/s)	87.84	83.00

^a SDSS ID: 3307-54970-529^b SDSS ID: 3214-54866-429**Table 2**
Derived Stellar Parameters

	Medium Resolution			High Resolution			
	T_{eff} (K)	$\log g$ (cgs)	[Fe/H]	T_{eff} (K)	$\log g$ (cgs)	ξ (km/s)	[Fe/H]
SDSS J1322+0123	5466 (150)	3.12 (0.35)	−3.32 (0.20)	5008 (100)	1.95 (0.20)	1.95 (0.20)	−3.64 (0.05)
SDSS J1204+1201	5894 (150)	2.66 (0.35)	−3.41 (0.20)	5467 (100)	3.20 (0.20)	1.50 (0.20)	−4.34 (0.05)

Table 3
Equivalent-Width Measurements

	SDSS J1322+0123					SDSS J1204+1201	
Ion	λ (Å)	χ (eV)	$\log gf$	W (mÅ)	$\log \epsilon$ (X)	W (mÅ)	$\log \epsilon$ (X)
Na I	5889.950	0.00	0.108	62.8	2.30	39.0	2.28
Na I	5895.924	0.00	−0.194	61.9	2.58	30.3	2.41
Mg I	3829.355	2.71	−0.208	98.5	4.01
Mg I	3832.304	2.71	0.270	132.3	4.22	89.6	3.62
Mg I	4167.271	4.35	−0.710	9.1	4.35
Mg I	4702.990	4.33	−0.380	13.6	4.18
Mg I	5172.684	2.71	−0.450	105.0	4.19	63.5	3.78
Mg I	5183.604	2.72	−0.239	117.2	4.23	64.1	3.59
Mg I	5528.405	4.34	−0.498	12.9	4.27
Al I	3961.520	0.01	−0.340	37.6	1.49
Si I	3905.523	1.91	−1.092	106.5	4.14	71.8	3.88
Ca I	4226.730	0.00	0.244	103.8	2.52	77.1	2.42
Ca I	4283.010	1.89	−0.224	16.2	3.17
Ca I	4434.960	1.89	−0.010	16.8	2.97
Ca I	4454.780	1.90	0.260	24.6	2.92
Ca I	6162.170	1.90	−0.089	18.8	3.06
Ca I	6439.070	2.52	0.470	12.0	2.96
Ca II	3933.663	0.00	0.105	728.3	2.35
Sc II	4246.820	0.32	0.240	47.7	−0.86	13.6	−0.78
Sc II	4314.083	0.62	−0.100	20.4	−0.73
Ti II	3759.291	0.61	0.280	124.6	1.80
Ti II	3761.320	0.57	0.180	116.8	1.67
Ti II	3813.394	0.61	−2.020	20.9	1.62
Ti II	3913.461	1.12	−0.420	48.6	1.17
Ti II	4012.396	0.57	−1.750	44.6	1.78
Ti II	4025.120	0.61	−1.980	21.8	1.58
Ti II	4290.219	1.16	−0.930	31.4	1.36
Ti II	4337.914	1.08	−0.960	37.0	1.41
Ti II	4395.031	1.08	−0.540	52.4	1.26
Ti II	4399.765	1.24	−1.190	22.9	1.51
Ti II	4443.801	1.08	−0.720	45.0	1.30
Ti II	4450.482	1.08	−1.520	14.8	1.42
Ti II	4468.517	1.13	−0.600	41.0	1.17	19.0	1.48
Ti II	4501.270	1.12	−0.770	37.7	1.26
Ti II	4533.960	1.24	−0.530	38.3	1.17
Ti II	4563.770	1.22	−0.960	30.1	1.41
Ti II	4571.971	1.57	−0.320	32.8	1.23
Cr I	4254.332	0.00	−0.114	45.4	1.33
Cr I	4274.800	0.00	−0.220	49.8	1.52
Cr I	4289.720	0.00	−0.370	26.5	1.21

Table 3 — *Continued*

Ion	λ (Å)	χ (eV)	$\log gf$	SDSS J1322+0123		SDSS J1204+1201	
				W (mÅ)	$\log \epsilon$ (X)	W (mÅ)	$\log \epsilon$ (X)
Cr I	5206.040	0.94	0.020	23.3	1.76
Cr I	5208.419	0.94	0.160	15.0	1.39	16.8	1.89
Mn I	4030.753	0.00	-0.480	58.8	1.28
Mn I	4033.062	0.00	-0.618	40.7	1.07
Mn I	4034.483	0.00	-0.811	45.2	1.34
Fe I	3727.619	0.96	-0.609	97.6	3.81
Fe I	3743.362	0.99	-0.790	96.8	4.00
Fe I	3753.611	2.18	-0.890	23.6	3.70
Fe I	3763.789	0.99	-0.221	109.3	3.76
Fe I	3765.539	3.24	0.482	41.0	3.89
Fe I	3767.192	1.01	-0.390	109.9	3.96	58.4	3.23
Fe I	3786.677	1.01	-2.185	41.0	4.04
Fe I	3787.880	1.01	-0.838	87.0	3.78
Fe I	3815.840	1.48	0.237	107.1	3.76	61.6	3.17
Fe I	3820.425	0.86	0.157	77.1	3.05
Fe I	3824.444	0.00	-1.360	118.1	3.97
Fe I	3825.881	0.91	-0.024	76.7	3.27
Fe I	3827.823	1.56	0.094	98.2	3.77
Fe I	3840.438	0.99	-0.497	103.1	3.85
Fe I	3841.048	1.61	-0.044	88.9	3.69
Fe I	3846.800	3.25	-0.020	19.4	3.90
Fe I	3849.967	1.01	-0.863	96.4	4.04
Fe I	3850.818	0.99	-1.745	59.4	3.94
Fe I	3856.372	0.05	-1.280	120.0	3.98
Fe I	3859.911	0.00	-0.710	85.8	3.27
Fe I	3865.523	1.01	-0.950	80.2	3.67
Fe I	3878.018	0.96	-0.896	85.8	3.72
Fe I	3878.573	0.09	-1.380	110.8	3.90	57.5	3.21
Fe I	3886.282	0.05	-1.080	65.3	3.08
Fe I	3887.048	0.91	-1.140	32.5	3.24
Fe I	3895.656	0.11	-1.668	95.2	3.78	42.8	3.15
Fe I	3899.707	0.09	-1.515	106.2	3.90
Fe I	3902.946	1.56	-0.442	86.8	3.96
Fe I	3917.181	0.99	-2.155	35.3	3.85
Fe I	3920.258	0.12	-1.734	98.1	3.92	41.4	3.19
Fe I	3922.912	0.05	-1.626	107.8	4.01	45.4	3.10
Fe I	3940.878	0.96	-2.600	26.4	4.07
Fe I	3949.953	2.18	-1.251	13.8	3.75
Fe I	3977.741	2.20	-1.120	22.3	3.90
Fe I	4005.242	1.56	-0.583	79.1	3.87
Fe I	4045.812	1.49	0.284	106.8	3.66	59.9	3.07
Fe I	4063.594	1.56	0.062	99.0	3.75	46.1	3.02
Fe I	4067.978	3.21	-0.470	11.8	4.04
Fe I	4071.738	1.61	-0.008	101.7	3.94	423.0	3.07
Fe I	4132.058	1.61	-0.675	74.5	3.88
Fe I	4134.678	2.83	-0.649	11.3	3.77
Fe I	4143.868	1.56	-0.511	75.7	3.68	28.3	3.18
Fe I	4147.669	1.48	-2.071	15.4	3.82
Fe I	4181.755	2.83	-0.371	23.6	3.88
Fe I	4187.039	2.45	-0.514	31.9	3.77
Fe I	4187.795	2.42	-0.510	36.2	3.83
Fe I	4191.430	2.47	-0.666	26.7	3.84
Fe I	4199.095	3.05	0.156	26.9	3.67
Fe I	4202.029	1.49	-0.689	71.1	3.66
Fe I	4216.184	0.00	-3.357	36.0	3.90
Fe I	4222.213	2.45	-0.914	24.2	4.00
Fe I	4233.603	2.48	-0.579	29.0	3.81
Fe I	4250.119	2.47	-0.380	32.3	3.67
Fe I	4250.787	1.56	-0.713	79.6	3.97	17.3	3.07
Fe I	4260.474	2.40	0.077	69.0	3.86
Fe I	4271.154	2.45	-0.337	40.5	3.77
Fe I	4271.760	1.49	-0.173	91.8	3.66	50.9	3.27
Fe I	4282.403	2.18	-0.779	29.5	3.68
Fe I	4325.762	1.61	0.006	94.2	3.67	52.7	3.26
Fe I	4337.046	1.56	-1.695	34.6	4.00
Fe I	4375.930	0.00	-3.005	46.8	3.73
Fe I	4383.545	1.48	0.200	115.6	3.86	58.4	3.07
Fe I	4404.750	1.56	-0.147	92.6	3.71	45.1	3.18
Fe I	4415.122	1.61	-0.621	74.6	3.78
Fe I	4427.310	0.05	-2.924	49.3	3.75
Fe I	4447.717	2.22	-1.339	15.2	3.90
Fe I	4459.118	2.18	-1.279	22.4	4.00
Fe I	4461.653	0.09	-3.194	38.1	3.85

Table 3 — *Continued*

Ion	λ (Å)	χ (eV)	$\log gf$	SDSS J1322+0123		SDSS J1204+1201	
				W (mÅ)	$\log \epsilon$ (X)	W (mÅ)	$\log \epsilon$ (X)
Fe I	4476.019	2.85	-0.820	11.3	3.94
Fe I	4489.739	0.12	-3.899	14.4	4.02
Fe I	4494.563	2.20	-1.143	23.7	3.91
Fe I	4528.614	2.18	-0.822	41.5	3.94
Fe I	4531.148	1.48	-2.101	18.3	3.91
Fe I	4871.318	2.87	-0.362	20.5	3.79
Fe I	4872.137	2.88	-0.567	12.0	3.73
Fe I	4890.755	2.88	-0.394	21.6	3.86
Fe I	4891.492	2.85	-0.111	29.3	3.73
Fe I	4918.994	2.85	-0.342	19.3	3.71
Fe I	4920.503	2.83	0.068	36.5	3.67
Fe I	5006.119	2.83	-0.615	21.9	4.03
Fe I	5012.068	0.86	-2.642	32.6	4.04
Fe I	5051.634	0.92	-2.764	26.1	4.09
Fe I	5269.537	0.86	-1.333	98.2	4.11	32.6	3.29
Fe I	5328.039	0.92	-1.466	90.3	4.12
Fe I	5328.531	1.56	-1.850	18.0	3.70
Fe I	5371.489	0.96	-1.644	80.7	4.10
Fe I	5397.128	0.92	-1.982	65.6	4.06
Fe I	5405.775	0.99	-1.852	58.9	3.88
Fe I	5429.696	0.96	-1.881	62.0	3.94
Fe I	5434.524	1.01	-2.126	36.6	3.76
Fe I	5446.917	0.99	-1.910	54.9	3.86
Fe I	5455.609	1.01	-2.090	45.2	3.88
Fe I	5506.779	0.99	-2.789	16.0	3.91
Fe II	4233.170	2.58	-1.970	27.2	3.85
Fe II	4522.630	2.84	-2.250	9.3	3.84
Fe II	4583.840	2.81	-1.930	22.0	3.93
Fe II	4923.930	2.89	-1.320	41.6	3.81
Fe II	5018.450	2.89	-1.220	49.2	3.85
Co I	3845.468	0.92	0.010	46.0	1.68
Co I	3873.120	0.43	-0.660	55.3	1.97
Co I	3881.869	0.58	-1.130	28.4	2.07
Co I	3995.306	0.92	-0.220	28.9	1.55
Co I	4121.318	0.92	-0.320	35.3	1.77
Ni I	3452.880	0.11	-0.900	76.8	2.45
Ni I	3483.770	0.28	-1.120	64.5	2.48
Ni I	3492.960	0.11	-0.265	92.8	2.30
Ni I	3519.770	0.28	-1.422	58.9	2.63
Ni I	3524.540	0.03	0.007	110.7	2.40
Ni I	3566.370	0.42	-0.251	68.9	2.61
Ni I	3597.710	0.21	-1.115	68.8	2.48
Ni I	3783.520	0.42	-1.420	54.2	2.56
Ni I	3807.140	0.42	-1.220	59.6	2.47
Ni I	3858.301	0.42	-0.951	71.5	2.47
Ni I	5476.900	1.83	-0.890	18.3	2.75

Table 4
Abundances for Individual Species

Species	$\log \epsilon_{\odot}$ (X)	SDSS J1322+0123				SDSS J1204+1201			
		$\log \epsilon$ (X)	[X/Fe]	σ	N	$\log \epsilon$ (X)	[X/Fe]	σ	N
Li	1.05	1.70	...	0.15	1
C	8.43	5.28	+0.49 ^a	0.20	1	<5.54	< +1.45	...	1
Na I	6.24	2.44	-0.16	0.10	2	2.34	+0.44	0.05	2
Mg I	7.60	4.21	+0.25	0.05	7	3.66	+0.40	0.05	3
Al I	6.45	1.49	-1.32	...	1
Si I	7.51	4.14	+0.27	...	1	3.88	+0.71	...	1
Ca I	6.34	2.93	+0.23	0.08	6	2.42	+0.42	...	1
Ca II	6.34	2.35	+0.35	...	1
Sc II	3.15	-0.79	-0.30	0.05	2	-0.78	+0.41	...	1
Ti II	4.95	1.42	+0.11	0.05	17	1.48	+0.87	...	1
Cr I	5.64	1.44	-0.56	0.08	5	1.89	+0.59	...	1
Mn I	5.43	1.23	-0.56	0.07	3
Fe I	7.50	3.86	-3.64 ^b	0.01	88	3.16	-4.34 ^b	0.02	21
Fe II	7.50	3.86	-3.64 ^b	0.02	5
Co I	4.99	1.81	+0.46	0.08	6
Ni I	6.22	2.50	-0.08	0.05	10	2.61	+0.73	...	1
Sr II	2.87	-2.01	-1.24	0.20	2	< -1.55	< -0.08	...	1

Table 4 — *Continued*

Species	$\log \epsilon_{\odot} (X)$	SDSS J1322+0123				SDSS J1204+1201			
		$\log \epsilon (X)$	$[X/Fe]$	σ	N	$\log \epsilon (X)$	$[X/Fe]$	σ	N
Ba II	2.18	-2.76	-1.30	0.20	1	< -1.54	< +0.62	...	1

^a $[C/Fe]=+0.50$ using corrections of [Placco et al. \(2014b\)](#).^b $[FeI/H]$ and $[FeII/H]$ values**Table 5**
Example Systematic Abundance Uncertainties for SDSS J1322+0123

Elem	ΔT_{eff} +150 K	$\Delta \log g$ +0.2 dex	$\Delta \xi$ +0.2 km/s	σ_{tot} (dex)
Na I	0.15	-0.01	-0.03	0.18
Mg I	0.12	-0.03	-0.05	0.14
Al I	0.15	-0.02	-0.02	0.18
Si I	0.17	-0.03	-0.11	0.23
Ca I	0.11	-0.02	-0.03	0.14
Sc II	0.10	0.06	-0.02	0.14
Ti II	0.09	0.06	-0.03	0.12
Cr I	0.17	-0.02	-0.02	0.19
Mn I	0.20	-0.02	-0.03	0.21
Fe I	0.18	-0.02	-0.07	0.19
Fe II	0.03	0.07	-0.02	0.09
Co I	0.19	-0.02	-0.02	0.23
Ni I	0.22	-0.03	-0.09	0.24
Sr II	0.11	0.07	-0.03	0.16
Ba II	0.12	0.05	-0.01	0.16

Table 6
Ultra Metal-Poor Stars from the Literature

ID	Name	$[Fe/H]$	$[C/Fe]$	$\log \epsilon (C)$	$\log \epsilon (N)$ measured	$\log \epsilon (N)$ estimated ^b	Progenitor Mass (M_{\odot})	Energy ($\times 10^{51}$ erg)	Reference
1	SDSS J2209-0028	-4.00	+2.56	6.99	...	6.39	27.0	0.3	Spite et al. (2013)
2	HE 2139-5432	-4.02	+2.60 ^a	7.01	5.89	...	28.0	0.6	Yong et al. (2013a)
3	G77-61	-4.03	+2.49	7.00	6.40	...	27.0	0.3	Allen et al. (2012)
4	CS 30336-049	-4.03	+0.09 ^a	4.85	4.70	...	21.5	0.3	Yong et al. (2013a)
5	HE 1424-0241	-4.05	+0.63	5.01	...	4.41	21.5	0.3	Yong et al. (2013a)
6	HE 0057-5959	-4.08	+0.86	5.21	5.90	...	27.0	0.3	Yong et al. (2013a)
7	SDSS J0140+23	-4.09	+1.57	5.91	...	5.31	27.0	0.3	Yong et al. (2013a)
8	HE 2239-5019	-4.15	+1.80	< 5.98	< 6.38	...	15.0	10.0	Hansen et al. (2014)
9	HE 1310-0536	-4.15	+2.53 ^a	6.72	< 6.88	...	10.9	0.3	Hansen et al. (2014)
10	CD-38 245	-4.15	-0.09 ^a	4.19	4.75	...	21.5	0.3	Yong et al. (2013a)
11	SDSS J1204+1201	-4.34	< +1.45	< 5.54	...	< 4.94	10.6	0.9	This work
12	CS 22949-037	-4.38	+1.73 ^a	5.78	5.95	...	27.0	0.3	Roederer (2013)
13	HE 0233-0343	-4.68	+3.32	7.23	< 5.95	...	11.9	0.3	Hansen et al. (2014)
14	HE 0557-4840	-4.75	+1.66 ^a	5.30	< 5.40	...	10.9	0.6	Masseron et al. (2012)
15	SDSS J1742+2531	-4.80	+3.63	7.26	...	6.66	21.5	0.3	Bonifacio et al. (2015)
16	SDSS J1029+1729	-4.99	< +0.70	< 4.20	< 3.10	...	10.6	0.9	Caffau et al. (2011a)
17	SDSS J1313+0019	-5.00	+2.96	6.39	6.29	...	27.0	0.3	Frebel et al. (2015)
18	SDSS J1035+0641	< -5.07	> +3.55	6.90	...	6.30	23.0	0.6	Bonifacio et al. (2015)
19	HE 0107-5240	-5.54	+2.69 ^a	5.58	3.80	...	20.5	0.6	Christlieb et al. (2002)
20	HE 1327-2326	-5.65	+3.48	6.26	5.93	...	21.5	0.3	Frebel et al. (2005)
21	SMSS J0313-6708	< -7.80	> +5.39	6.02	< 3.63	...	41.0	1.2	Bessell et al. (2015)

^a Using corrections of [Placco et al. \(2014b\)](#).^b Estimated from $[C/N]=0$. See text for details.**Table 7**
Changes Applied to the Literature Data

Case #	Constraint
(i)	$[C/Fe] - 0.5$
(ii)	$[C/Fe] - 1.0$
(iii)	$[N/Fe] - 0.5$
(iv)	$[N/Fe] - 1.0$

Table 7 — *Continued*

Case #	Constraint
(v)	$[\text{N}/\text{Fe}] + 0.5$
(vi)	$[\text{N}/\text{Fe}] + 1.0$
(vii)	$[\text{N}/\text{Fe}] + 2.0$
(viii)	no carbon/nitrogen
(ix)	no carbon
(x)	no nitrogen